The Astrophysical Journal, 968:129 (10pp), 2024 June 20 https://doi.org/10.3847/1538-4357/ad414a
© 2024. The Author(s). Published by the American Astronomical Society.
OPEN ACCESS

Detection of Accretion Shelves Out to the Virial Radius of a Low-mass Galaxy with JWST

Charlie Conroy[1], Benjamin D. Johnson[1], Pieter van Dokkum[2], Alis Deason[3], Sandro Tacchella[4,5], Sirio Belli[6], William P. Bowman[2], Rohan P. Naidu[7,9], Minjung Park[1], Roberto Abraham[8], and Razieh Emami[1]
[1] Center for Astrophysics | Harvard & Smithsonian, 60 Garden Street, Cambridge, MA 02138, USA
[2] Department of Astronomy, Yale University, New Haven, CT 06511, USA
[3] Institute for Computational Cosmology, Department of Physics, Durham University, Durham, DH1 3LE, UK
[4] Kavli Institute for Cosmology, University of Cambridge, Madingley Road, Cambridge, CB3 0HA, UK
[5] Cavendish Laboratory, University of Cambridge, 19 JJ Thomson Avenue, Cambridge, CB3 0HE, UK
[6] Dipartimento di Fisica e Astronomia, Università di Bologna, Bologna, Italy
[7] MIT Kavli Institute for Astrophysics and Space Research, 77 Massachusetts Avenue, Cambridge, MA 02139, USA
[8] Department of Astronomy & Astrophysics, University of Toronto, 50 St. George Street, Toronto, ON M5S 3H4, Canada
Received 2023 November 6; revised 2024 March 31; accepted 2024 April 14; published 2024 June 20

Abstract

We report the serendipitous discovery of an extended stellar halo surrounding the low-mass galaxy Ark 227 ($M_* = 5 \times 10^9\, M_\odot$; $d = 35$ Mpc) in deep JWST NIRCam imaging from the Blue Jay Survey. The F200W–F444W color provides robust star–galaxy separation, enabling the identification of stars at very low density. By combining resolved stars at large galactocentric distances with diffuse emission from NIRCam and Dragonfly imaging at smaller distances, we trace the surface-brightness and color profiles of this galaxy over the entire extent of its predicted dark matter halo, from 0.1 to 100 kpc. Controlled *N*-body simulations have predicted that minor mergers create "accretion shelves" in the surface-brightness profile at large radius. We observe such a feature in Ark 227 at 10–20 kpc, which, according to models, could be caused by a merger with total mass ratio 1:10. The metallicity declines over this radial range, further supporting the minor merger scenario. There is tentative evidence of a second shelf at $\mu_V \approx 35$ mag arcsec^{-2} extending from 50 to 100 kpc, along with a corresponding drop in metallicity. The stellar mass in this outermost envelope is $\approx 10^7\, M_\odot$. These results suggest that Ark 227 experienced multiple mergers with a spectrum of lower-mass galaxies—a scenario that is broadly consistent with the hierarchical growth of structure in a cold-dark-matter-dominated universe. Finally, we identify an ultra-faint dwarf associated with Ark 227 with $M_* \approx 10^5\, M_\odot$ and $\mu_{V,e} = 28.1$ mag arcsec^{-2}, demonstrating that JWST is capable of detecting very-low-mass dwarfs to distances of at least $\sim$30 Mpc.

Unified Astronomy Thesaurus concepts: Galaxy stellar halos (598)

1. Introduction

The cold dark matter (CDM) cosmological model predicts that structure forms "bottom-up," in which larger, more massive dark matter halos grow from the assimilation of many smaller halos. This process is most clearly observed in the spectacular faint tidal features and complex stellar halos observed in the Milky Way and other galaxies of comparable or greater masses (e.g., Majewski et al. 2003; Mihos et al. 2005; Belokurov et al. 2006; McConnachie et al. 2009; Martínez-Delgado et al. 2010; Bailin et al. 2011; Ibata et al. 2014; Rejkuba et al. 2014; Duc et al. 2015; Okamoto et al. 2015; Crnojević et al. 2016; Merritt et al. 2016; Monachesi et al. 2016; Harmsen et al. 2017; Naidu et al. 2020; Smercina et al. 2020).

CDM predicts that this assimilation process is approximately scale-free, such that dwarf mass halos should form from the accretion of still lower mass objects (Tarumi et al. 2021). In fact, observations of dwarf halos may even provide a probe of the nature of dark matter on these scales (Deason et al. 2022). However, the relation between galaxy mass and dark matter halo mass is very steep and uncertain at low masses. It is therefore unclear if the predicted bottom-up, accretion-driven formation process is observable in the form of tidal debris and stellar halos at the scale of dwarf galaxies. Observations at the dwarf scale have identified merging dwarf galaxies (Paudel et al. 2018), tidal debris (Martínez-Delgado et al. 2012; Strader et al. 2012; Kado-Fong et al. 2020), and extended material that may or may not be accretion in origin (e.g., Jang et al. 2020; Chiti et al. 2021).

Hydrodynamic simulations predict that in situ processes associated with bursty stellar feedback can drive stars born in dwarf galaxies to halo-like orbits (e.g., El-Badry et al. 2016; Kado-Fong et al. 2022). The bursty feedback is more common at early times, when the metallicity was lower. The stars on halo-like orbits therefore tend to be lower metallicity than the inner regions. The existence of metal-poor stars in the outskirts of dwarf galaxies is not in itself evidence of the hierarchical assembly process acting at the dwarf scale. This alternative channel for stellar halo formation has frustrated efforts to interpret stellar populations in the outskirts of dwarf galaxies (e.g., Chiti et al. 2021).

The spatial distribution of the most distant halo stars surrounding dwarf galaxies may break these degeneracies. Hierarchical merger models predict accretion shelves in the surface-brightness profiles of dwarfs that are directly related to the mass ratio of the merger (Amorisco 2017; Deason et al.

[9] NASA Hubble Fellow.

Original content from this work may be used under the terms of the Creative Commons Attribution 4.0 licence. Any further distribution of this work must maintain attribution to the author(s) and the title of the work, journal citation and DOI.

2022). Furthermore, in situ models seem unable to populate stars to a large fraction of the virial radius, unlike accretion scenarios (e.g., Kado-Fong et al. 2022). Surface-brightness measurements of a dwarf galaxy to its virial radius should therefore provide strong constraints on the physical origin of its stellar halo.

In this paper, we present serendipitous observations of the stellar halo of the galaxy Ark 227 observed by JWST as part of the Blue Jay Survey in the COSMOS field (S. Belli et al. 2024, in preparation). The sensitivity of JWST imaging allows us to trace the stellar halo of this galaxy to its dark matter halo virial radius. The observed surface-brightness and metallicity profiles suggest that this galaxy's stellar halo was built from the assimilation of smaller-mass galaxies, providing a dramatic example of hierarchical assembly at the dwarf scale.

Magnitudes reported in this paper adopt the AB zero-point system (Oke & Gunn 1983).

2. Data and Methods

2.1. JWST Imaging and "Discovery" of Ark 227

The Blue Jay Survey is a Cycle 1 JWST program (GO 1810; PI: Belli). The primary scientific objective of the program is to obtain deep spectra of a mass-selected sample of galaxies at cosmic noon ($1.7 < z < 3.5$). The NIRSpec microshutter array was used to obtain $R \approx 1000$ spectra of 150 galaxies with three medium-resolution gratings over two separate pointings. Parallel observations were obtained with NIRCam in a variety of filters of varying depths. The filters and associated exposure times are F090W (92 minutes), F115W (184 minutes), F150W (368 minutes), F200W (368 minutes), F277W (276 minutes), F356W (368 minutes), and F444W (368 minutes). Details of the program will be described in S. Belli et al. (2024, in preparation).

The orientation constraints of the NIRSpec observations resulted in one of the NIRCam modules being placed southwest of the available Hubble Space Telescope (HST)/CANDELS data in the COSMOS field. To our surprise, a nearby dwarf galaxy also happens to reside just southwest of the CANDELS-COSMOS field. We initially viewed this foreground dwarf with some dismay, as the imaging in this module is badly "contaminated" with not only the unresolved light from Ark 227 but also the resolved starlight associated with its stellar halo. While we were visually inspecting the mosaic far from Ark 227, we noticed a large number of point sources with a common color (which happened to be green in the adopted color map). Tracing these green dots across the mosaic, we realized that they appeared to be associated with Ark 227. As we will argue below, these green dots are the stellar halo of Ark 227 and are present throughout the entire NIRCam mosaic.

Ark 227 (PGC 28923; Arakelian 1975) is a dwarf galaxy with red colors and elliptical morphology. Its redshift is 1793 km s^{-1}. There is no reliable distance measurement in the literature. Leroy et al. (2019) adopt a Hubble flow-based distance of 26 Mpc to infer a stellar mass of $2.7 \times 10^9\, M_\odot$. We present a (much more accurate) TRGB-based distance of 35 Mpc below, with a corresponding larger stellar mass. Adopting the stellar mass–halo mass relation from Behroozi et al. (2013) implies a halo mass of $2 \times 10^{11}\, M_\odot$ and hence a virial radius of ≈100 kpc. Galactic extinction toward Ark 227 is small; we adopt $E(g-r) = 0.016$ from Schlafly & Finkbeiner (2011). Its environment has not been studied in detail, but it is not known to be associated with any bright galaxy (Polzin et al. 2021).

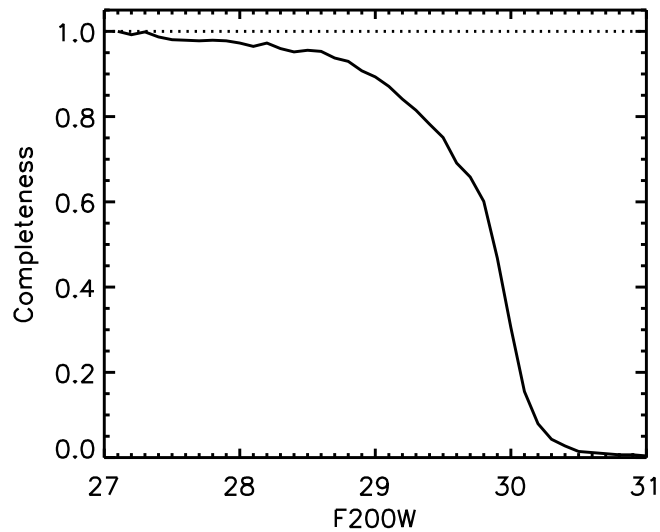

Figure 1. Photometric completeness vs. point-source magnitude in the F200W filter. Completeness was determined by injecting artificial stars into the imaging data.

2.2. Data Reduction and Photometry

The imaging used a four-point dither pattern dictated by the spectroscopic program. The individual exposures were processed using the "jwst" data-reduction pipeline version 1.9.4 with CRDS context map "jwst_1039.pmap." The exposures were then astrometrically aligned using a reference catalog derived from HST imaging registered to Gaia (Gaia Collaboration et al. 2018; Mowla et al. 2019) before final mosaicing. Sources were detected on a stack of the F150W and F200W mosaics via the Source Extractor program (Bertin & Arnouts 1996), and circular aperture photometry was measured in all bands for the sources at the detection coordinates in several apertures, including 1 and 2 pixel radii. A subset of sources (described below) were passed through the `forcepho` program (B. Johnson et al. 2024, in preparation), which fits point-spread function (PSF)-convolved Sérsic profiles to the multiband exposure level images of each source, enabling measurements of source sizes (half-light radii), colors, and total integrated fluxes.

2.3. Completeness

We now turn to an estimate of the completeness of the photometric catalog as a function of stellar flux and position from the center of Ark 227. We use the standard technique of injecting artificial stars into the imaging data. Specifically, 640,000 fake stars were injected into the mosaic-level imaging data and given normally distributed colors of F150W–F200W $= -0.25 \pm 0.05$ and F200W–F444W $= -1.5 \pm 0.1$. We then ran these fake stars through the detection and selection algorithms (as described in previous subsection), and applied the same set of selection criteria described in the next section. The completeness is computed as the fraction of fake stars recovered and passing the selection criteria.

The result of this exercise is shown in Figure 1 as a function of input F200W magnitude. The completeness drops rapidly at F200W >29.7. This is due mostly to our use of the F200W–

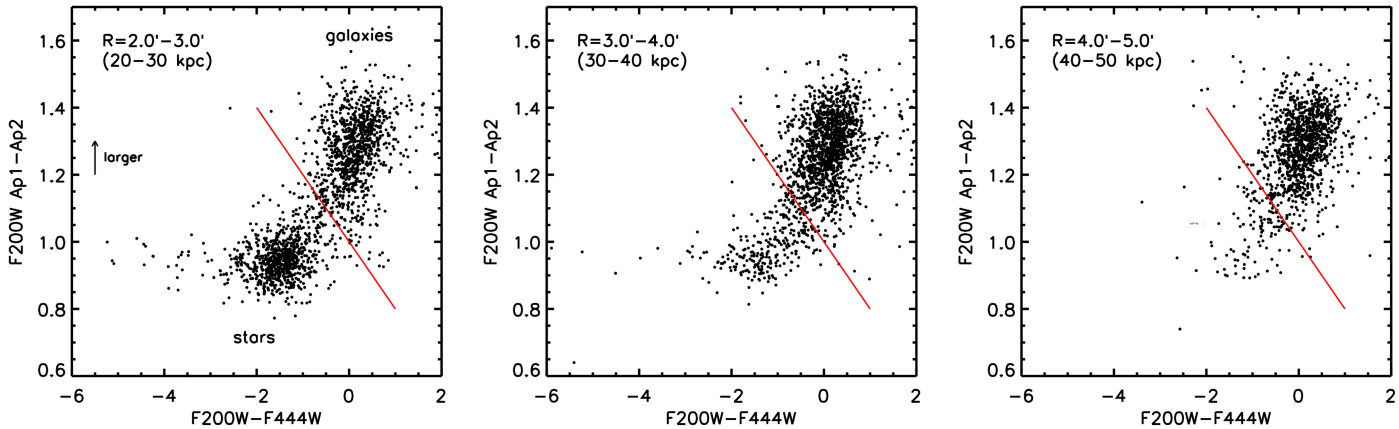

Figure 2. "Pseudo-size" vs. color diagrams at increasing distance from the center of Ark 227. The F200W–F444W color provides strong separation between stars and galaxies and is measured in fixed apertures of 2 pixel radii. The difference in F200W magnitudes measured in a 1 and 2 pixel aperture (0.″03 and 0.″06; Ap1–Ap2) is shown on the *y*-axis and is a proxy for the size of the source. The red line is our initial selection of star-like objects. Sources below this line are passed through the light profile-fitting algorithm `forcepho`.

F444W color in selecting stars combined with the fact that stars are very blue in this color. In essence, the depth is limited by the F444W imaging. We found no significant radial variation in the completeness over the range probed in our resolved star measurements.

We apply these completeness corrections to the analysis below.

2.4. Selection of Stars

We experimented with a variety of diagnostic diagrams in order to separate stars from galaxies. The most useful diagnostic is a combination of short- and long-wavelength photometry (in particular, F200W–F444W) and a proxy for the object size (see also Warfield et al. 2023, who advocate a short- and long-wavelength JWST filter for efficient star–galaxy separation). For the latter, we adopted the difference between 1 and 2 pixel aperture (0.″03 and 0.″06) photometry in the F200W band (Ap1–Ap2). This band is our deepest and so has the best signal-to-noise ratio. For point sources, the difference in aperture photometry is a measure of the point-spread function and hence should be approximately a constant. Stars have blue colors in rest-frame F200W–F444W because both filters are redward of the 1.5 μm peak of cool stars. Galaxies are intrinsically redder in this color because they are a composite stellar population that includes very cool stars. However, a larger effect is redshifting: at $z > 0.3$ the F200W filter is sampling flux blueward of the 1.5 μm spectral energy distribution peak, which results in substantially redder F200W–F444W colors.

The resulting diagnostic diagram is shown in Figure 2 at three annuli of increasing distance from Ark 227. This diagram clearly shows two distinct populations: compact sources at F200W–F444W ≈ -1.75 and extended sources at F200W–F444W $\gtrsim -1$. The relative proportion of sources in the blue and red loci change markedly from the inner to outer regions of Ark 227, strongly suggesting that the blue sources are stars associated with Ark 227.

Our first selection of stars consists of sources falling below the red line in Figure 2; specifically, Ap1–Ap2 < -0.2 (F200W–F444W) $+ 1.0$. This line was determined by eye to separate the two populations. This is a generous selection, including a number of sources that are likely not stars. All objects satisfying this selection are passed through the profile-fitting program `forcepho`.

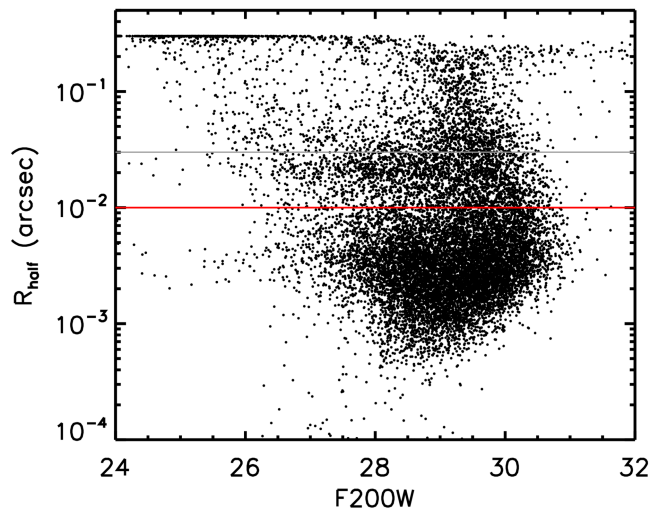

Figure 3. Size vs. F200W magnitude for all sources selected as "star-like" in Figure 2. Sizes and magnitudes are determined from profile fitting. The gray line is the size of a NIRCam pixel in the SW module. Our sample of star-like point sources is comprised of all objects below the red line.

Figure 3 shows the half-light radius versus total F200W magnitude for all objects satisfying the star-like selection in Figure 2. The JWST NIRCam pixel size is 0.″03 in the short-wavelength (SW) module; this scale is included as a gray line in Figure 3. Most objects are very compact and are effectively unresolved. We adopt a selection of $R_{\rm half} < 0.''01$ to isolate stars from resolved objects (shown as a red line in the figure). This selection removes 27% of star-like objects with F200W < 30 and distances $>0.'5$ from the center of Ark 227.

In Figure 3 there is a locus of sources at sizes of $\approx 0.''003$ and F200W < 26 that are Milky Way foreground stars (this population extends to F200W ≈ 20). A second locus of sources with $R_{\rm half} \approx 0.''03$ have colors and a spatial distribution very different from the sources below the red line. These sources are likely compact background galaxies.

Figure 4 shows a color–magnitude diagram (CMD) in F150W and F200W filters for the star-like point sources passing the selection criteria defined in Figures 2 and 3. The CMDs are shown in three annuli at increasing distance from

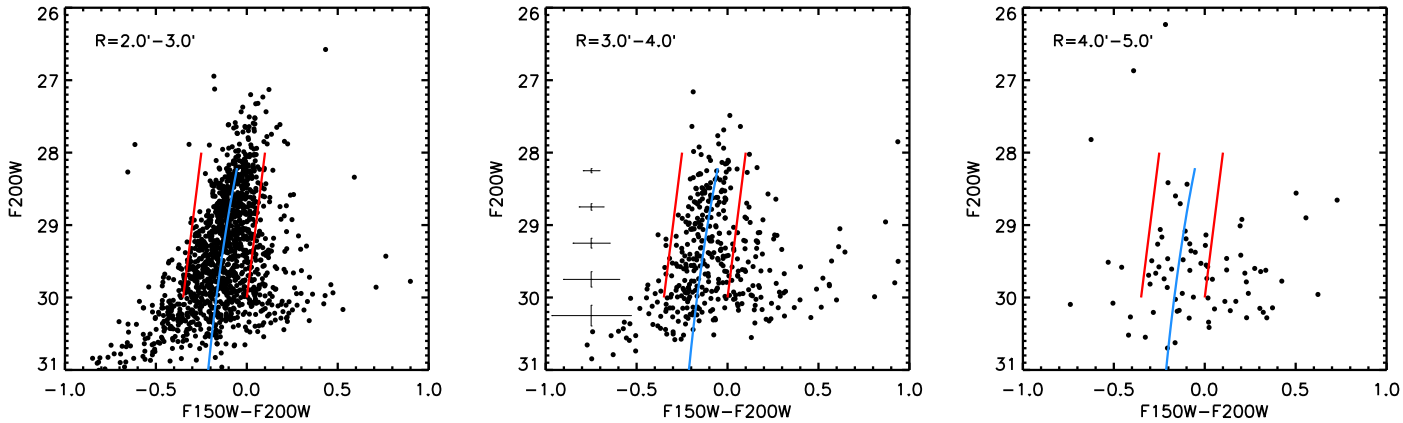

Figure 4. Color–magnitude diagrams of star-like point sources at increasing separation from the center of Ark 227. Red lines demarcate our final selection of stars. A 10 Gyr [Fe/H] = −1 MIST isochrone is shown at a distance of 35 Mpc (blue lines). Typical uncertainties are shown in the middle panel as a function of magnitude.

Ark 227. A 10 Gyr model red giant branch at [Fe/H] = −1.0 is overplotted as a blue line at an assumed distance of 35 Mpc. Average uncertainties are shown as a function of magnitude in the middle panel. The CMD of these star-like point sources is clearly consistent with the evolved giants of an old metal-poor stellar population.

Our final selection of stars associated with Ark 227 consists of the objects bounded by the nearly vertical red lines in the CMD, restricted to 28 < F200W < 30. The color selection ensures that the stars have RGB-like colors. The bright limit rejects very bright AGB stars but also limits potential interlopers, such as globular clusters and foreground (Milky Way) dwarf stars. The faint limit is set by the photometric depth. This selection removes another 22% of stars brighter than F200W = 30 and >0.′5 from the center of Ark 227.

In summary, our selection for stars associated with Ark 227 is based on the selections shown in Figures 2, 3, and 4 and is designed to select point sources with RGB colors. Our final sample contains 6044 stars. The resulting distribution of stars is shown in Figure 5, along with the F200W mosaic. Also shown in this figure are the circular annuli within which the surface brightness will be measured.

The CMD shows a sharp tip of the RGB (TRGB) location at F200W ≈ 28.2. To explore this further, we show the stellar luminosity function in Figure 6. We include a comparison to a model luminosity function of a 10 Gyr, [Fe/H] = −1.0 stellar population from the MIST isochrones. We have placed the model at 35 Mpc and added magnitude-dependent uncertainties comparable to the data. The distance was fit by eye; more sophisticated fitting is not warranted given that the uncertainty on the distance is dominated by the dependence of the RGB tip on metallicity: for [Fe/H] = −0.75, −1.0, and −1.5, the RGB tip is F200W = −4.73, −4.55, and −4.23, respectively. An uncertainty on the distance modulus of 0.25 mag corresponds to a distance uncertainty of 12%. We therefore adopt a distance to Ark 227 of 35 ± 4 Mpc.

The CMD of stars in the outermost radial bin in Figure 4 looks noticeably different compared to the inner two bins. In particular, there are fewer bright stars at or above the TRGB defined by the inner bins. This issue is explored in Figure 7, where we show the luminosity function of stars at >4′. This scale corresponds to >50 kpc, i.e., the three outermost points in the surface-brightness profile in Figure 8 below. We include two model luminosity functions (LFs) for a 10 Gyr population at [Fe/H] = −1.0 and −1.5. The metal-rich model, which fits the inner radii data well (see Figure 6), is clearly a poor fit to the data in this outermost bin. In contrast, the metal-poor model fits both the slope of the LF and the TRGB, which is ≈0.4 mag fainter than the metal-rich case. As we will see below, there is tentative evidence that this outermost population of stars is also bluer than the inner population, which supports the idea that this population is more metal-poor than the inner population.

2.5. Surface-brightness Measurements

Our primary goal is to measure the surface-brightness profile of Ark 227. At $R < 10''$, we directly measure the diffuse light of Ark 227 from JWST NIRCam imaging. At $R > 35''$, we measure resolved star photometry of Ark 227. In the latter case, we convert the observed flux measured over the magnitude range 28 < F200W < 30 to an integrated flux. We do this by employing a 10 Gyr [FeH] = −1 isochrone from v2.3 of the MIST models (Choi et al. 2016). The fraction of light in the observed magnitude range is 26%; we use this fraction to correct our observed flux to an estimate of the total flux (this fraction varies from 23% to 26% over the range −1.5 < [Fe/H] < −0.5). In order to convert our total F200W fluxes to the more commonly reported V-band flux, we adopt an integrated color of V − F200W = 0.74, appropriate for a 10 Gyr, [FeH] = −1 isochrone.

As discussed in Section 3.4, we identified an ultra-faint dwarf (UFD) galaxy in the halo of Ark 227. The stars associated with this dwarf are removed before measuring the surface-brightness profile of Ark 227.

We assess the level of contamination in our star selection in several ways. First, we use an empirically calibrated model of star counts in the Milky Way (Girardi et al. 2005) to estimate contamination from foreground stars. We find a likely contamination from Milky Way stars that pass our CMD selection to be at the level of $\mu_V \approx 38$ mag arcsec^{-2}.

Second, we employ data from the JADES Survey (Eisenstein et al. 2023), which achieves photometric depths comparable to Blue Jay. We select three ≈10 arcmin^2 regions and use aperture photometry to select star-like candidates. We apply the same CMD selection and magnitude limits as used in the Blue Jay data. Since forcepho photometry is not available, we employ a stricter selection in the pseudo-size–color diagram. Specifically, we select stars in a box defined by −3.0 < F200W–F444W < −0.5 and 0.85 < (Ap1–Ap2) < 1.0. If we analyze the sources identified this way in the same

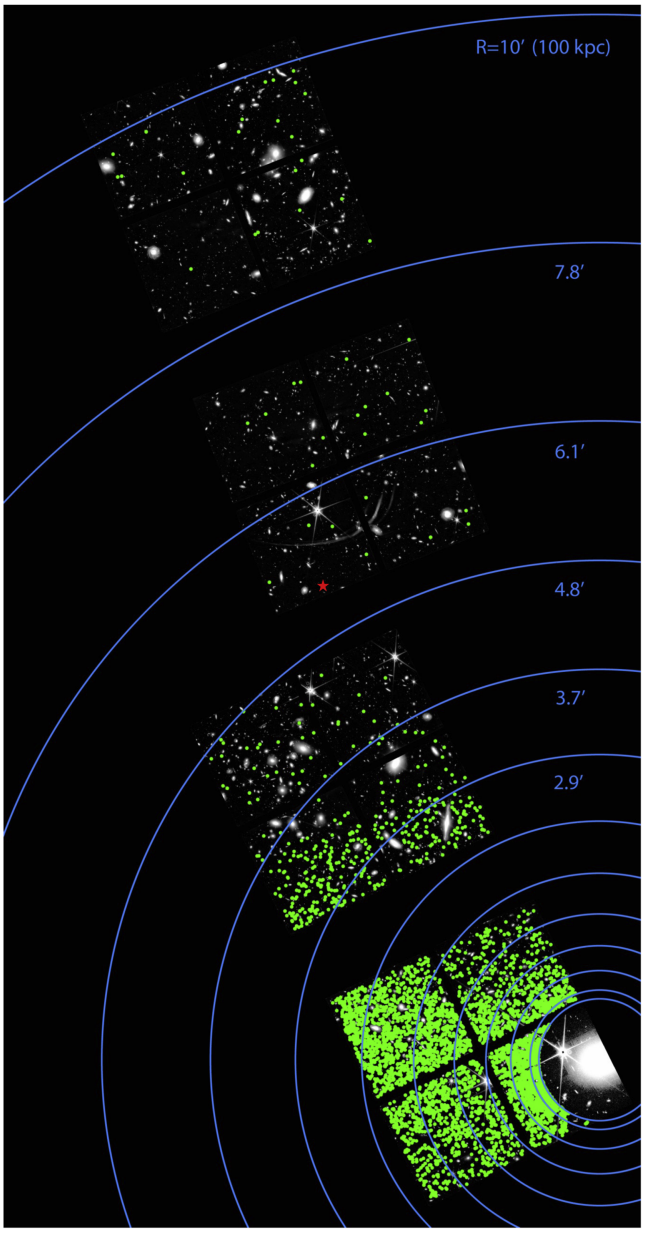

Figure 5. Mosaic of the Blue Jay data in the F200W filter. Ark 227 is clearly visible in the lower-right corner. Annuli from which surface-brightness measurements are made via resolved stars are shown in blue. Our final sample of star candidates associated with Ark 227 is shown as green points. The red star indicates the position of the ultra-faint dwarf.

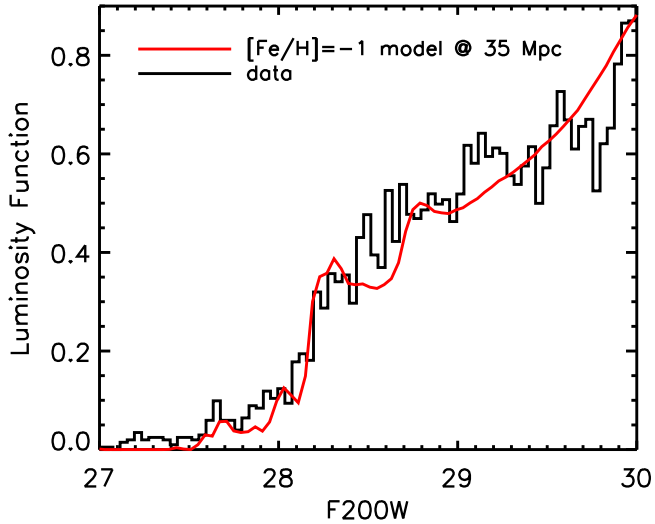

Figure 6. Luminosity function (LF) of stars associated with Ark 227. The red line shows a model LF assuming a distance of 35 Mpc from the MIST isochrones.

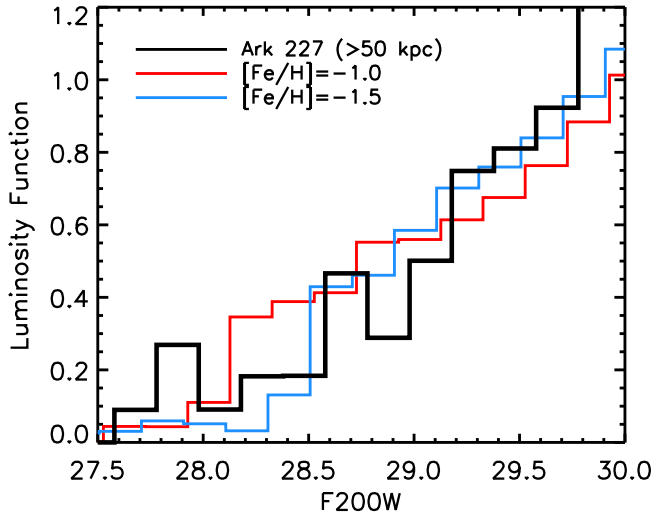

Figure 7. LF of stars at >4.′7 (>50 kpc). This corresponds to stars in the last three bins of the surface-brightness profile in Figure 8. Predicted LFs for 10 Gyr populations at [Fe/H] = −1.0 and −1.5 are included. The latter is a much better fit to the data.

manner as the Ark 227 sources, we arrive at surface-brightness limits of $\mu_V = 37.4$, 36.1, and 35.9 mag arcsec^{-2}.

Inspection of the images reveals that many of the star-like sources identified in JADES are associated with nearby ($z \lesssim 0.2$) bright galaxies. It is likely that these sources are unresolved massive globular clusters. The JADES fields with a greater number of spectroscopically confirmed galaxies at $z < 0.2$ correspond to fields with higher densities of star-like sources, further supporting this conclusion. We therefore regard extragalactic globular clusters as the dominant source of contamination in our analysis. Their visible association with bright galaxies should enable their identification and removal. Though we leave a full treatment of this next step to future work, we visually inspected the Blue Jay data and found that in the outermost radial bin (>7.′8) as many as 50% of the sources could plausibly be associated with foreground galaxies. We took a conservative approach and removed 50% of the sources in this last radial bin. In the next two radial bins (4.′8–7.′8), we saw little evidence for associations and so made no corrections. Owing to these complications, we regard measurements of surface brightness at $\mu_V \gtrsim 35$ mag arcsec^{-2} as tentative.

2.6. Dragonfly Imaging

At high surface densities it is relatively straightforward to measure the diffuse emission from a galaxy, while at very low surface densities, where stellar crowding is not a concern, it is conventional to measure surface brightness from resolved star counts. At the boundary of these two regimes challenges abound. At one end, crowding makes resolved star measurements increasingly challenging. At the other end, the diffuse flux level is so faint that special techniques and/or observatories are required to avoid systematic errors from scattered light, flat-fielding, etc. Our current reduction of the

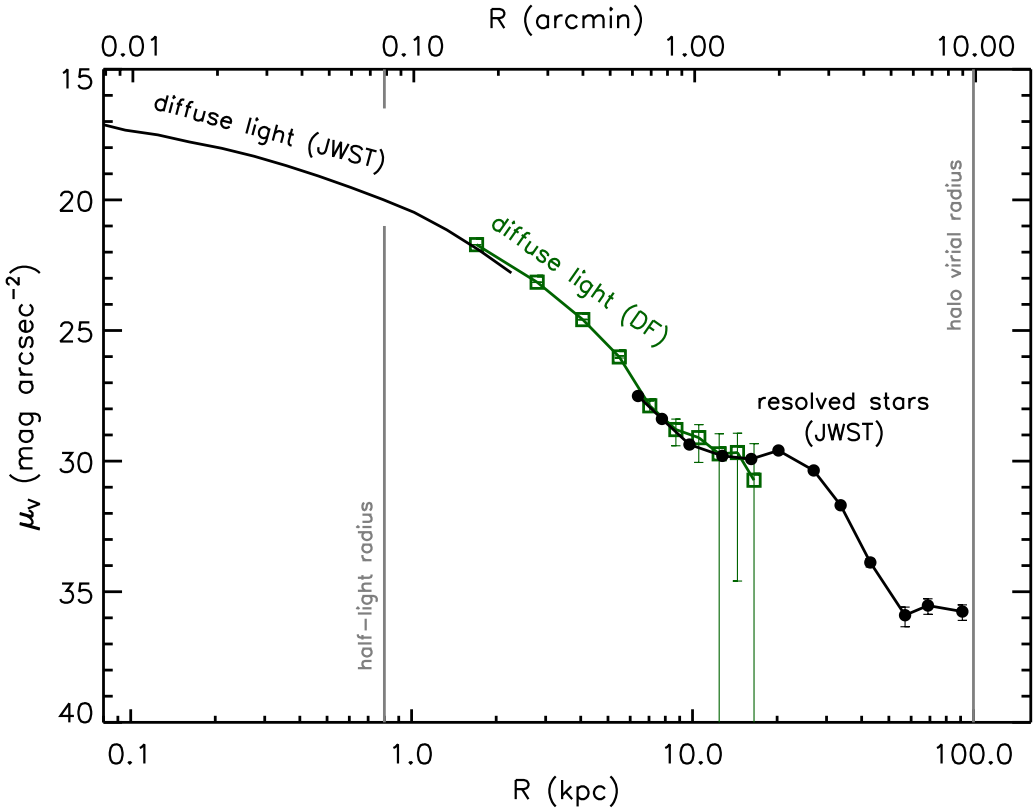

Figure 8. Surface-brightness profile of Ark 227 from 0.1 to 100 kpc, measured via diffuse light from JWST NIRCam imaging, diffuse light from Dragonfly (DF) imaging, and resolved starlight from JWST NIRCam photometry. The half-light and halo virial radii are indicated with vertical gray lines. A TRGB-based distance of 35 Mpc was adopted to convert angles into projected distances. Uncertainties are based on Poisson statistics. We regard the second shelf at $\mu_V > 35$ mag arcsec^{-2} as tentative, owing to the small numbers of stars and contamination from background sources.

JWST NIRCam data does not deliver reliable diffuse flux measurements beyond $R \approx 10''$. A 12th-magnitude star resides $22''$ from the center of Ark 227, further complicating efforts at measuring low-surface-brightness features via diffuse emission.

To bridge the resolved and diffuse emission regimes, we turn to the Dragonfly Telephoto Array, a special-purpose observatory designed for low-surface-brightness imaging (Abraham & van Dokkum 2014). Ark 227 is close in projection to the unrelated edge-on spiral galaxy NGC 3044 at a distance of 23 Mpc, and it was serendipitously observed in a deep Dragonfly (DF) observation of that galaxy. The DF data for NGC 3044 are described in Gilhuly et al. (2022); they reach 3σ surface-brightness limits of 29.8 mag arcsec^{-2} in g and 29.1 mag arcsec^{-2} in r. They were rereduced with the latest DF pipeline (W. Bowman et al. 2024, in preparation).

Stars and other compact objects were subtracted from the DF data with the multi-resolution filtering technique (van Dokkum et al. 2020), using Legacy Survey imaging as input to the model (see Gilhuly et al. 2022). The 12th-magnitude star is saturated in the Legacy imaging but not in the DF data; it was subtracted with a custom wide-angle PSF created from other bright stars in the field. Residuals of bright subtracted objects were masked, as described in van Dokkum et al. (2020). Surface-brightness profiles in g and r were measured from the filtered image using aperture photometry, taking missing flux in masked regions properly into account. We find no evidence for asymmetries in the light distribution, but we note that this is difficult to assess in the vicinity of the bright star and other relatively bright stars to the north of Ark 227. Uncertainties were determined from the empirical variations in the background in empty areas of the images. We translate the g-band magnitudes to V band assuming $g - V = 0.42$, appropriate for our fiducial isochrone.

3. Results

3.1. Surface-brightness Profile

Figure 8 shows the final surface-brightness profile for Ark 227 from 0.1 to 100 kpc. We combine diffuse-light measurements from JWST NIRCam and DF imaging with estimates from resolved star counts at large radius. The half-light radius and approximate dark matter halo virial radius are indicated with gray lines. The agreement between the three distinct tracers of the surface-brightness profile is excellent and provides a good check that none of the probes contains serious systematic errors. The surface-brightness profile spans 18 magnitudes, for a total change in intensity of $\approx 10^7$.

There are three distinct regimes in the surface-brightness profile. At $R \lesssim 6$ kpc the profile is smoothly declining and is reasonably well described by a single Sérsic model. At $10 \lesssim R \lesssim 50$ kpc the surface-brightness profile flattens to a level of $\mu_V \approx 30$ mag arcsec^{-2} and then drops rapidly over $20 \lesssim R \lesssim 50$ kpc. We refer to this morphology as a shelf in the brightness profile. Similar accretion shelves have been identified in resolved star maps of more massive galaxies (Bailin et al. 2011; Fardal et al. 2012; Smercina et al. 2023), including the apparent "pile up" of debris at the edge of the shelf (Smercina et al. 2023).

Finally, at $R \gtrsim 50$ kpc the surface-brightness flattens again, with no sign of truncation to the limit of our data (although

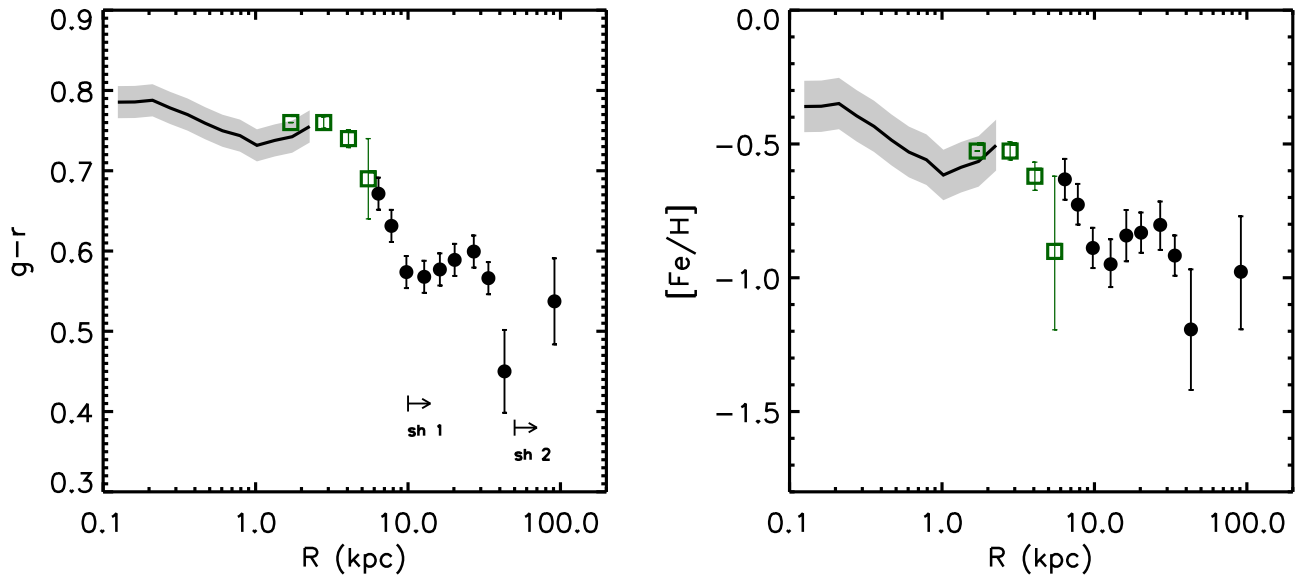

Figure 9. Left panel: Color profile of Ark 227. The diffuse emission measured from NIRCam imaging (solid line) is converted to $g-r$ from the observed F115W–F200W color assuming a color conversion of 0.7 mag. The diffuse emission measured from DF imaging (green squares) is obtained in g and r filters. The resolved star data is converted from a mean RGB color to an integrated $g-r$ based on isochrones. Right panel: Metallicity profile estimated from the measured diffuse and resolved colors. The color and metallicity abruptly decrease at the locations where the surface-brightness profile flattens, indicated by the arrows and "sh 1," "sh 2" in the left panel.

measurements at $\mu \gtrsim 35$ mag arcsec^{-2} are tentative, for reasons discussed in Section 2.5). Assuming a stellar mass-to-light ratio of $M/L_V = 2$, the mass within 10 kpc is $5.2 \times 10^9\, M_\odot$, within $10 < R < 50$ kpc is $2.0 \times 10^8\, M_\odot$, and at >50 kpc is $1.0 \times 10^7\, M_\odot$. We return to the potential origins of these distinct regimes below.

3.2. Color and Metallicity Profile

The left panel of Figure 9 shows the $g-r$ color profile of Ark 227. At the smallest radii the color is estimated directly from the diffuse emission in JWST NIRCam imaging using the F115W and F200W filters. We then adopt a fixed color term of $g-r = \mathrm{F115W–F200W} + 0.70$ based on integrated colors from 10 Gyr isochrones. This color term is nearly constant over a wide range in metallicity, varying by ± 0.05 over $-2 < [\mathrm{Fe/H}] < +0.5$. The DF data were obtained in g and r filters and so $g-r$ colors can be readily measured from those data. At the largest distances where resolved star data are employed, we use a 10 Gyr $[\mathrm{Fe/H}] = -1$ isochrone to determine an offset between the RGB F115W–F200W color and the integrated $g-r$ color of 0.36. This is only approximate because the color variation seen in the data is likely a reflection of underlying metallicity variation, and the mean luminosity of stars changes slightly with distance.

The right panel of Figure 9 shows the estimated stellar metallicity profile of Ark 227. For the integrated light measurements we use color–metallicity relations from isochrones to translate the observed F115W–F200W and $g-r$ colors into metallicities. For the DF $g-r$ data, we have applied a small offset of -0.03 in the color before converting to metallicities in order to provide a slightly better match to the metallicity at smaller scales. This offset could be due to zero-point uncertainties in the photometry, or small offsets in the color–metallicity relations in different bands. For the resolved stars, we compute the mean luminosity in each annulus and construct an RGB F115W–F200W color versus metallicity relation at the associated mean luminosity. We then use the observed color to estimate a metallicity.

Precise metallicities will require either spectroscopy (which will be very challenging at these depths) or additional photometric bands. The key takeaway from Figure 9 is that the shelves in the surface-brightness profile correspond to abrupt declines in the color and therefore metallicity profiles. This strongly suggests that the distinct features in the light profile correspond to distinct stellar populations.

3.3. Comparison to Hierarchical Growth Models

In this section, we compare our results to cosmologically motivated merger models. We employ the framework presented in Deason et al. (2022) in which idealized dark-matter-only mergers are run with the `GADGET-2` code. Stars are assigned to dark matter halos according to a stellar mass–halo mass relation and a particle-tagging technique with an observationally motivated size–mass relation. Deason et al. (2022) focused on the merger histories of dwarfs with halo masses $10^{10}\, M_\odot$. Here we consider models more appropriate for Ark 227 with $M_{\rm halo} = 10^{11}\, M_\odot$ and a halo concentration of $c = 10$.

The left panel of Figure 10 shows the predicted surface-brightness profiles of the satellite debris for merger models in which the total mass ratios are 1:3, 1:5, 1:10, and 1:16 (the total mass includes baryonic and dark matter). There are two important features that vary with mass ratio: the slope of the surface-brightness profile becomes flatter for higher mass ratios, and the location of the sharp cutoff extends to much larger radius for higher mass ratios. The origin of these trends is a consequence of the competing effects of tidal stripping and dynamical friction (see discussion in Amorisco 2017; Deason et al. 2022). Dynamical friction scales with the mass ratio, such that more equal-mass mergers result in a much more efficient sinking of the satellite to the center of the host, where the satellite is then tidally stripped. In contrast, for high mass ratios, dynamical friction is inefficient, and so the satellite spends much of its time in the outskirts of the host. Tidal

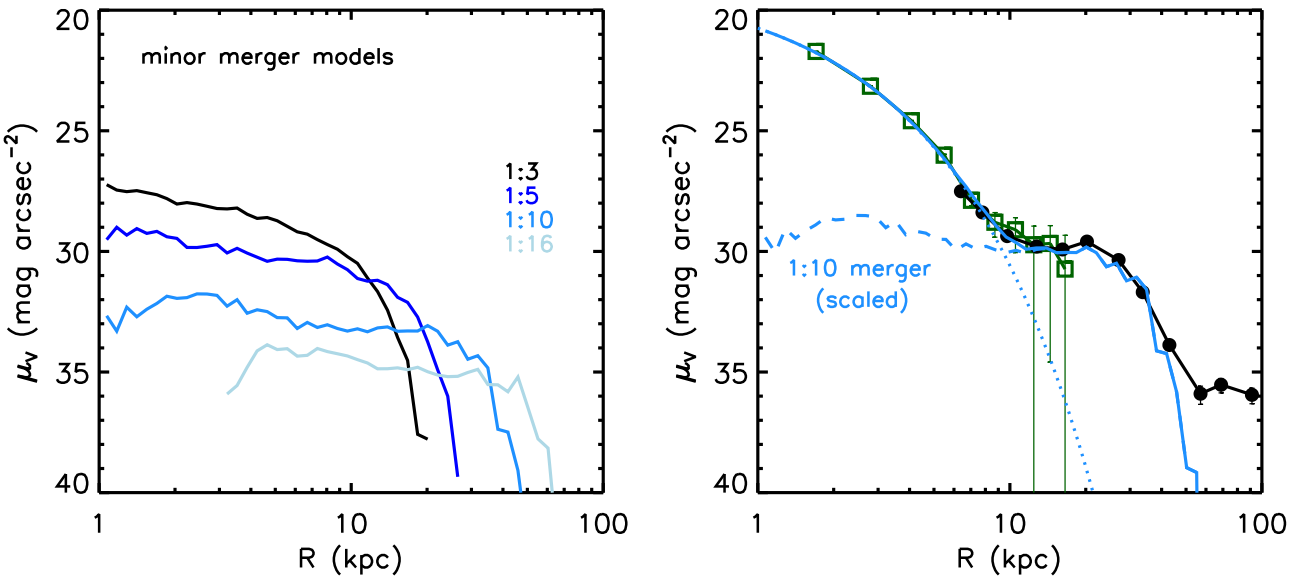

Figure 10. Left panel: surface-brightness profiles of satellite debris resulting from minor mergers, with merger ratios indicated in the figure. Notice that higher mass ratios result in a more extended surface-brightness profile. Right panel: comparison between the data and a model in which the host (represented by a dotted line) undergoes a 1:10 merger (dashed line); the combined model profile is shown as a solid blue line. The merger is scaled up by a factor of 20 compared to the models in the left panel. Either Ark 227 underwent many such mergers or the adopted stellar mass of the satellite merger was larger than assumed in the default model.

stripping still occurs near the satellite orbit pericenter, but that material is then able to travel to the outskirts, where it spends most of its time. The properties of the initial satellite orbit have a surprisingly small effect on the resulting surface-brightness profile (Amorisco 2017). The largest effect is at small radius, which is difficult to observe because of the overwhelming effect of the host stellar density.

The right panel of Figure 10 shows a comparison between the data and a merger model. The model was constructed by combining a by-eye Sérsic fit to the inner light profile (dotted line) with a 1:10 total mass ratio merger model (dashed line). The latter was scaled upward in luminosity by a factor of 20. This model does an excellent job of reproducing the shelf in the surface-brightness profile at 10–50 kpc. The second, tentative, shelf at >50 kpc would seem to require a merger with a total mass ratio >1:16, which is the most extreme mass ratio we were able to simulate. A lower satellite halo concentration may also produce a more extended distribution (Amorisco 2017). Exploration of higher mass ratios and a wider range of satellite properties is required to understand the nature of the tenuous outer shelf in Ark 227.

The observed shelf at ∼10 kpc is much more luminous than the corresponding 1:10 total mass ratio merger. We emphasize that the model adds stars to the simulation by hand, and so the normalization is not a strong prediction of the model, in contrast to the shape, which *is* a strong prediction and is set by the total mass ratio of the merger. There are at least two possible explanations for the large offset. Ark 227 could have experienced many 1:10 mergers, resulting in an aggregate luminosity comparable to the data. This seems unlikely because cosmological simulations do not predict such a large number of 1:10 mergers. It would also be difficult to imagine such a large number mergers producing a very strong shelf feature.

A second possibility is that the satellite galaxy occupying the $10^{10}\,M_\odot$ halo is more massive than assumed by Deason et al (2022). The stellar mass in the shelf is $\approx 2\times 10^8\,M_\odot$, or approximately 10% of the total stellar mass of Ark 227. Deason et al. (2022) adopted a fairly steep stellar mass–halo mass relation where $M_* \propto M_h^{1.6}$. Either this relation instead has a power-law index closer to 1.0, or the satellite accreted by Ark 227 happens to be overluminous for its halo mass. With only a single object it is difficult to reach a strong conclusion on this point. Observations of additional dwarf halos are necessary to resolve this issue.

3.4. An Ultra-faint Dwarf Galaxy Associated with Ark 227

Visual inspection of the spatial distribution of point sources revealed a strong overdensity of sources 50 kpc (5′) from the center of Ark 227. There are 17 sources within a few arcsec—a spatial density far higher than the background stellar halo at this projected separation.

Figure 11 shows the spatial distribution (left panel) and CMD (right panel) of these 17 sources. Unlike the analysis in earlier sections, a CMD filter has not been applied to this sample; the only selection is a half-light size smaller than 0.″01. A strong, roughly circular distribution of sources is clearly visible. Notice that there are no background halo stars within this 20″ × 20″ cutout. The half-light radius of these sources is 1.″4 and is indicated by the smaller circle. Twice the half-light radius is indicated with a larger circle. The right panel shows the CMD along with isochrones for [Fe/H] = −1.5 and −2.0. The sources are clearly consistent with a metal-poor population at the distance of Ark 227. The surface brightness within the half-light radius is $\mu_{V,e} = 28.1$ mag arcsec^{-2}.

Assuming that these sources are associated with Ark 227, the physical half-light size is 230 pc. Summing up the flux from the 17 sources and accounting for the unresolved flux from fainter sources implies a luminosity of $M_V = -7.0$ and a stellar mass of $M_* \approx 10^5\,M_\odot$, assuming $M/L_V = 2$. Assuming the stellar mass–metallicity relation of Local Group dwarf galaxies, we expect a metallicity for this system of [Fe/H]≈ −2 (Kirby et al. 2013). The size and luminosity are consistent with the properties of UFD galaxies (Simon 2019); we therefore consider this object a UFD associated with Ark 227, and refer to it as Ark 227-UFD1.

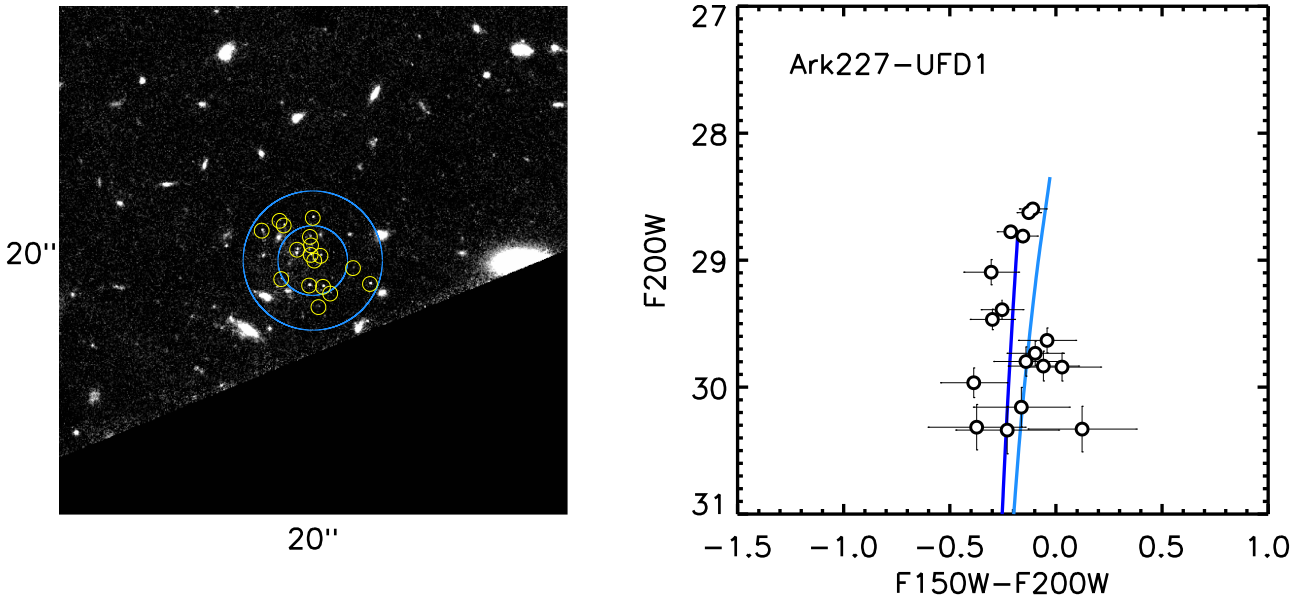

Figure 11. The ultra-faint dwarf Ark 227-UFD1. Left panel: 20″ cutout centered on the dwarf, which happens to fall toward the edge of the field. Yellow circles show all sources satisfying the point-source selection in Figure 3. One and two times the half-light radius are indicated by the circles. Right panel: CMD of all point sources within 2″ of Ark 227-UFD1. The light and dark blue lines show isochrones for [Fe/H] = −1.5 and −2.0, respectively. Ark 227-UFD1 has a half-light size of $1\farcs4 \approx 230$ pc, a surface brightness of 28.1 mag arcsec^{-2}, and a stellar mass of $\approx 10^5\,M_\odot$.

We calculate the effective area covered by our two NIRCam pointings and for which we could have detected a UFD. We removed the lowermost module from this estimation as there are too many point sources to be able to easily identify an overdensity of stars associated with a dwarf. The source detection map was used to identify and mask large galaxies from the effective area. We find an effective area of ≈12 arcmin^2. The total area subtended by the halo virial radius is 300 arcmin^2. The effective area of our search represents ≈one-twenty-fifth of the total halo, suggesting that Ark 227 may harbor several dozen UFDs at $M_* \sim 10^5\,M_\odot$.

4. Summary and Discussion

In this paper, we reported the serendipitous discovery of at least one—and possibly two—accretion shelves in the halo of the dwarf galaxy Ark 227 ($M_* = 5 \times 10^9\,M_\odot$; $M_{\rm halo} \approx 2 \times 10^{11}\,M_\odot$). Deep JWST NIRCam imaging provided robust star–galaxy separation to $m_{\rm AB} \approx 30$, and enabled us to trace the surface-brightness profile of Ark 227 to a limit of $\mu_V \approx 35$ mag arcsec^{-2} to this galaxy's predicted dark matter halo virial radius at 100 kpc. One accretion shelf is clearly detected at $\mu_V \approx 30$ mag arcsec^{-2} at 10–20 kpc from the center of Ark 227. A second, tentative shelf is detected at $\mu_V \approx 35$ mag arcsec^{-2} at 50–100 kpc. Stellar colors versus radius provide evidence for abrupt changes in metallicity at the location of these shelves.

Accretion shelves are generic predictions of hierarchical structure formation (e.g., Amorisco 2017; Deason et al. 2022). Their amplitude and location provide fairly direct information on the properties of the accreted satellite, or satellites: The amplitude is determined by the stellar mass ratio of the merger and the location by the halo mass ratio. In Ark 227, comparison to models suggests that Ark 227 experienced at least two minor mergers: a 1:10 merger with a galaxy of stellar mass $10^8\,M_\odot$ and [Fe/H]≈ −0.8, and a >1:20 merger with a galaxy of mass $10^7\,M_\odot$ and [Fe/H]≈ −1.2. The stellar masses and metallicities of these accreted dwarfs are consistent with the observed mass–metallicity relation of intact dwarfs measured in the local Universe (Kirby et al. 2013). These deep JWST data have enabled the most detailed reconstruction of the hierarchical assembly of a dwarf galaxy to date.

Stellar halos have been traced to the virial radii of the Milky Way (Deason et al. 2018), M31 (Ibata et al. 2007), and now Ark 227. If we assume that it is common for stars to populate the entire extent of dark matter halos, we can estimate the fraction of the sky that is filled with stellar halos. For this estimate, we use the empirical model from Behroozi et al. (2019), which populates galaxies in a large cosmological volume. Halos hosting galaxies with $\log M_*/M_\odot = 9$ within 35 Mpc cover 5%–15% of the sky. Extending this to all halos above $\log M_*/M_\odot = 8$ and within 70 Mpc, the covering fraction reaches 20%–30% of the sky. These numbers imply that the existence of a stellar halo in the foreground of one of the few well-studied extragalactic deep fields, while surprising to us, is not an exceptionally rare configuration.

With a stellar mass of $5 \times 10^9\,M_\odot$, Ark 227 lies at the upper end of the dwarf-galaxy mass scale. Deason et al. (2022) simulated predicted stellar halos for galaxies with stellar masses of $10^7\,M_\odot$, finding that the signatures of hierarchical assembly may be present at the level of $\mu_V \sim 35$ mag arcsec^{-2}. This limit has not yet been breached for very-low-mass dwarfs, but we have shown here that JWST imaging is a unique and efficient tool for such searches. Future observations of nearby, isolated dwarf galaxies with JWST should place strong constraints on the accretion histories of low-mass galaxies.

Acknowledgments

This work is based on observations made with the NASA/ESA/CSA JWST. The data were obtained from the Mikulski Archive for Space Telescopes at the Space Telescope Science Institute, which is operated by the Association of Universities for Research in Astronomy, Inc., under NASA contract NAS 5-03127 for JWST. These observations are associated with program GO 1810. The computations in this paper were run on

the FASRC Cannon cluster supported by the FAS Division of Science Research Computing Group at Harvard University.

C.C. acknowledges support from JWST-GO-1810. S.B. is supported by the ERC Starting Grant "Red Cardinal," GA 101076080. R.P.N. acknowledges support for this work provided by NASA through the NASA Hubble Fellowship grant No. HST-HF2-51515.001-A awarded by the Space Telescope Science Institute, which is operated by the Association of Universities for Research in Astronomy, Incorporated, under NASA contract NAS5-26555.1. R.E. acknowledges the support from grant Nos. 21-ATP21-0077, NSF AST-1816420, and HST-GO-16173.001-A as well as the Institute for Theory and Computation at the Center for Astrophysics.

Software: `MIST` (Choi et al. 2016), `forcepho` (B. Johnson et al. 2024, in preparation)

ORCID iDs

Charlie Conroy https://orcid.org/0000-0002-1590-8551

References

Abraham, R. G., & van Dokkum, P. G. 2014, PASP, 126, 55
Amorisco, N. C. 2017, MNRAS, 464, 2882
Arakelian, M. A. 1975, CoBAO, 47, 3
Bailin, J., Bell, E. F., Chappell, S. N., Radburn-Smith, D. J., & de Jong, R. S. 2011, ApJ, 736, 24
Behroozi, P., Wechsler, R. H., Hearin, A. P., & Conroy, C. 2019, MNRAS, 488, 3143
Behroozi, P. S., Wechsler, R. H., & Conroy, C. 2013, ApJ, 770, 57
Belokurov, V., Zucker, D. B., Evans, N. W., et al. 2006, ApJL, 642, L137
Bertin, E., & Arnouts, S. 1996, A&AS, 117, 393
Chiti, A., Frebel, A., Simon, J. D., et al. 2021, NatAs, 5, 392
Choi, J., Dotter, A., Conroy, C., et al. 2016, ApJ, 823, 102
Crnojević, D., Sand, D. J., Spekkens, K., et al. 2016, ApJ, 823, 19
Deason, A. J., Belokurov, V., & Koposov, S. E. 2018, ApJ, 852, 118
Deason, A. J., Bose, S., & Fattahi, A. 2022, MNRAS, 511, 4044
Duc, P.-A., Cuillandre, J.-C., Karabal, E., et al. 2015, MNRAS, 446, 120
Eisenstein, D. J., Willott, C., Alberts, S., et al. 2023, arXiv:2306.02465
El-Badry, K., Wetzel, A., Geha, M., et al. 2016, ApJ, 820, 131
Fardal, M. A., Guhathakurta, P., & Gilbert, K. M. 2012, MNRAS, 423, 3134
Gaia Collaboration, Brown, A. G. A., Vallenari, A., Prusti, T., et al. 2018, A&A, 616, A1
Gilhuly, C., Merritt, A., Abraham, R., et al. 2022, ApJ, 932, 44
Girardi, L., Groenewegen, M. A. T., Hatziminaoglou, E., & da Costa, L. 2005, A&A, 436, 895
Harmsen, B., Monachesi, A., Bell, E. F., et al. 2017, MNRAS, 466, 1491
Ibata, R., Martin, N. F., Irwin, M., et al. 2007, ApJ, 671, 1591
Ibata, R. A., Lewis, G. F., McConnachie, A. W., et al. 2014, ApJ, 780, 128
Jang, I. S., de Jong, R. S., Minchev, I., et al. 2020, A&A, 640, L19
Kado-Fong, E., Greene, J. E., Greco, J. P., et al. 2020, AJ, 159, 103
Kado-Fong, E., Sanderson, R. E., Greene, J. E., et al. 2022, ApJ, 931, 152
Kirby, E. N., Cohen, J. G., & Guhathakurta, P. 2013, ApJ, 779, 102
Leroy, A. K., Sandstrom, K. M., Lang, D., et al. 2019, ApJS, 244, 24
Majewski, S. R., Skrutskie, M. F., Weinberg, M. D., & Ostheimer, J. C. 2003, ApJ, 599, 1082
Martínez-Delgado, D., Gabany, R. J., Crawford, K., et al. 2010, AJ, 140, 962
Martínez-Delgado, D., Romanowsky, A. J., Gabany, R. J., et al. 2012, ApJL, 748, L24
McConnachie, A. W., Irwin, M. J., Ibata, R. A., et al. 2009, Natur, 461, 66
Merritt, A., van Dokkum, P., Abraham, R., & Zhang, J. 2016, ApJ, 830, 62
Mihos, J. C., Harding, P., Feldmeier, J., & Morrison, H. 2005, ApJL, 631, L41
Monachesi, A., Bell, E. F., & Radburn-Smith, D. J. 2016, MNRAS, 457, 1419
Mowla, L. A., van Dokkum, P., Brammer, G. B., et al. 2019, ApJ, 880, 57
Naidu, R. P., Conroy, C., Bonaca, A., et al. 2020, ApJ, 901, 48
Okamoto, S., Arimoto, N., Ferguson, A. M. N., et al. 2015, ApJL, 809, L1
Oke, J. B., & Gunn, J. E. 1983, ApJ, 266, 713
Paudel, S., Smith, R., Yoon, S. J., Calderón-Castillo, P., & Duc, P.-A. 2018, ApJS, 237, 36
Polzin, A., van Dokkum, P., Danieli, S., Greco, J. P., & Romanowsky, A. J. 2021, ApJL, 914, L23
Rejkuba, M., Harris, W. E., Greggio, L., et al. 2014, ApJL, 791, L2
Schlafly, E. F., & Finkbeiner, D. P. 2011, ApJ, 737, 103
Simon, J. D. 2019, ARA&A, 57, 375
Smercina, A., Bell, E. F., Price, P. A., et al. 2020, ApJ, 905, 60
Smercina, A., Bell, E. F., Price, P. A., et al. 2023, ApJL, 949, L37
Strader, J., Seth, A. C., & Caldwell, N. 2012, AJ, 143, 52
Tarumi, Y., Yoshida, N., & Frebel, A. 2021, ApJL, 914, L10
van Dokkum, P., Lokhorst, D., Danieli, S., et al. 2020, PASP, 132, 074503
Warfield, J. T., Richstein, H., Kallivayalil, N., et al. 2023, RNAAS, 7, 23